

Electronic Mechanisms on the Iso-Structural Phase Transition in Fe-Mn Solid Solution

Wei Liu,^{1,2} Xiangyan Li,¹ Yichun Xu,¹ Yange Zhang,¹ Wenliang Li,³ Q. F. Fang,¹ Xuebang Wu,^{1,*} Yunfeng Liang,^{4,1,*} Caetano R. Miranda,^{5,*} Chuan-lu Yang,² C. S. Liu¹

¹Key Laboratory of Materials Physics, Institute of Solid State Physics, Chinese Academy of Sciences, P. O. Box 1129, Hefei 230031, China

²School of Physics and Optoelectronics Engineering, Ludong University, Yantai 264025, China

³College of Energy Engineering, Xinjiang Institute of Engineering, Urumqi 830091, China

⁴Department of Systems Innovation, the University of Tokyo, Tokyo 113-8656, Japan

⁵Instituto de Física, Universidade de São Paulo, CP 66318, São Paulo, SP 05315-970, Brazil

Abstract

Experiments overall suggested that dilute solid solution of manganese in body-centered cubic iron transforms from antiferromagnetic coupling into a ferromagnetic coupling at ~2 at.% Mn. Despite long-term theoretical studies, this phase transition is poorly understood, and the transition mechanism is still open. Based on DFT calculations with dense k -point meshes, we reveal that this "iso-structural" phase transition (IPT) occurs at 1.85 at.% Mn, originating from the shifting of $3d\ e_g$ level of Mn across the Fermi level and consequent intra-atomic electron transfer within $3d$ states of Mn. The IPT involves a sudden change of the bulk modulus accompanied by a small yet detectable change of the lattice constant, an inversion of magnetic coupling between solute Mn and Fe matrix, and a change in bonding strength between Mn and the first-nearest neighboring Fe atoms. Our interpretation of this IPT plays an enlightening role in understanding similar IPTs in other materials.

*Authors to whom correspondence should be addressed. Email address: xbwu@issp.ac.cn, liang@sys.t.u-tokyo.ac.jp, cmiranda@if.usp.br

In condensed matter physics, iso-structural phase transition (IPT) is particularly remarkable because of its unusual nature. For example, cerium (Ce) transforms from γ to α phase at ~ 8 kBar and ambient temperature with a volume collapse of $\sim 17\%$ and an electric-resistance drop of $\sim 40\%$ [1]. Experiments showed that IPTs in some materials are associated with intriguing phenomena, such as negative thermal expansion, giant magneto-elastic coupling, and large piezoelectric response, indicating potential technological applications [2-4]. Great efforts have been made in studying the IPT mechanisms for more than a half-century. Some studies concentrated on the role of phonon dynamics in these IPTs [5,6], while others concentrated on electronic origin. It was found that the electronic valence transition of rare-earth elements leads to the IPTs in YbGaGe [2], YbInCu₄ [7], Eu(Pd_{1-x}Au_x)₂Si₂ [8] and SmS [9]. However, it has not been fully understood about the electronic origin of some other prototypical IPTs, including the $\gamma \rightarrow \alpha$ Ce transition and the insulator \rightarrow metal transition of V₂O₃ [10]. This is because experimental measurements were obviously inconsistent with the valence transition model and meanwhile could not offer detailed information to interpret the electronic process during these IPTs [11, 12]. From a theoretical viewpoint, a reasonable description of these IPTs needs accurately calculating correlation effects by treating the many-body N -electron configuration [13-15], which is beyond density-functional theory (DFT). The electronic density of states (DOS) of Ce in either phase calculated by DFT did not reproduce the famous three-peak structure of experimental spectra [12,16]. The mechanism of the insulator \rightarrow metal transition of V₂O₃ has been under debate so far [17,18]. Furthermore, current miscellaneous DFT methods, as well as merged methods with DFT, cannot produce two solutions (phases) for these materials and carry out transitions between them within a single available computational framework.

On the other hand, experiments suggested that a phase transition in body-centered cubic (bcc) Fe-Mn alloy with increasing Mn concentration [19]. Neutron diffraction measurements yield the μ_{Mn} values of -0.82 , 0 , and $0.6 \mu_{\text{B}}$, respectively at 0.79 , 1.5 , and 2.0 at.% Mn at room temperature [20-22]. At 2.0 at.% Mn and higher concentrations, all experiments presented positive μ_{Mn} values [19,23,24]. Long-term efforts have been made in theoretical studying the variation of μ_{Mn} with Mn concentration in bcc Fe-Mn alloy. Calculations of

linear-muffin-tin-orbital (LMTO) Green's function method showed that ferromagnetic (FM, $\mu_{\text{Mn}} > 0$) coupling and antiferromagnetic (AFM, $\mu_{\text{Mn}} < 0$) coupling states of Mn with bcc Fe matrix are both stable, and suggested that fluctuations between the two opposite states are responsible for the discrepancies in experimental μ_{Mn} data [25]. Recent DFT calculations using Perdew-Burke-Ernzerhof (PBE) functional indicated that the AFM coupling phase is the ground state, while the FM coupling phase, which may be referred to as the excited state, is in a rather flat local minimum in the energy landscape about 0.07 eV per Mn atom higher than the ground state [19,26]. Further calculations within special quasirandom structure model showed that the proportion of FM-Mn solutes is very small at dilute solution limit, but increases with increasing Mn concentration, which finally makes the average μ_{Mn} turn from negative to positive at ~6 at. % Mn [19]. These results provide a detailed scenario for the μ_{Mn} inversion as a function of Mn content and also an explanation for the much scattered theoretical μ_{Mn} results [27]. Two other theoretical studies predicted that the inversion of μ_{Mn} occurs respectively at ~13 at.% and ~1.5 at.% Mn in disordered bcc Fe-Mn alloy [28,29]. Within our reach, this phase transition might be firstly proposed by Mirzoev *et al.* based on Tight-Binding LMTO calculations [29]. Generally speaking, it is still known little about the phase transition, especially about the underlying mechanism, which motivates this study.

From early theoretical studies, Ce, Mn, and Fe are all at the cross-over between electron bonding behavior and magnetic moment formation [30]. For these metals, the electronic delocalization-localization transition can be induced by small perturbations, which ultimately modifies their properties. In this sense, similar IPT might occur in a "simpler" metallic system only with 3d narrow bands, e.g., the bcc Fe-Mn solid solution, so that the mechanism can be studied more easily. In this letter, the phase transition from AFM coupling to FM coupling between Mn and Fe matrix is demonstrated to occur at 1.85 at.% Mn from DFT calculations using a dense k -point mesh. This phase transition is confirmed to be an "iso-structural" one, involving a shift of localized state, electron transfer, change of bonding strength, and sudden jump of the bulk modulus. Our calculations present a detailed view of the electronic process in this IPT, which is essential for further understanding of the complex interplay between electronic and lattice degrees of freedom. Besides, we find an excited state in FM coupling

order at 1.39 at.% Mn [31]. This letter is arranged as follows. The variation of elastic and structural properties with solute content of seven Fe-X (X=3d transition metals) solid solutions are examined. Investigations on electronic structure and magnetism are made to explain the anomalous behavior in Fe-Mn alloy. An IPT is confirmed, and its mechanism is suggested. Enthalpy calculations are performed to address why only positive magnetic moments of Mn are detected in experiments at 1.85 at.% Mn and higher concentrations. Discussions on the excited state at 1.39 at.% Mn, high-pressure effect and Mn-cluster effect on this IPT are presented in the end.

All *ab initio* calculations are performed by the projector augmented wave method within DFT, as implemented in the Vienna *ab initio* simulation package (VASP) [32,33]. Exchange-correlation functionals are parameterized by Perdew and Wang (PW91) within the generalized gradient approximation [34], while the interpolation of the correlation part is done by Vosko-Wilk-Nusair (VWN) method [35]. The pseudopotential that treats semi core $3p^6$ as valence electrons is used for Mn, while the standard is used for all the other 3d elements. Detailed DFT settings can be found in Refs. [31,36]. Six different solute concentrations from 0.4 to 2.08 at.%, are considered by six different supercells that each has one solute besides Fe atoms. The dimensions of these supercells and the corresponding k -point meshes are listed in TABLE I. The much dense k -point meshes are necessary for accurately calculating forces on each atom and stress tensor. For the $3 \times 3 \times 4$ and $4 \times 4 \times 3$ bcc supercells, the length ratios of [100] (or [010]) edge versus [001] edge are set to be $3/4$ and $4/3$, respectively. For the $3 \times 2 \times 2$ tetragonal supercell [37], the length ratio of [100] edge versus [011] (or $[0\bar{1}1]$) edge is set to be $3/2\sqrt{2}$. Although there are slight residual stresses in these supercells due to the "ideal" edge-length ratio settings, they do not affect our study on the IPT mechanism of Fe-Mn alloy. The tetrahedron smearing method with Blöchl corrections is employed in calculating electronic and magnetic properties. An arithmetic scheme is employed to extract bulk modulus B of bcc Fe based solid solutions from the *ab initio* calculated stresses [31,36]. The calculated B and lattice constant a of α -Fe are listed in TABLE I. Hydrostatic strain (HS) is set to be $\pm 0.1\%$ to calculate B . The bulk modulus difference, ΔB , is obtained from the difference between the B value of Fe-X alloy with respect to the reference (α -Fe) with the

same set of supercell and k -point mesh. Similarly, we calculate the lattice constant difference, Δa , of the Fe-X alloy. The elastic energy E_{ela} is calculated by the total energy of a Fe-X alloy under -0.1% HS subtracting that one at zero strain. The substitution energy of a solute, E_{sub} , under zero strain, is defined in Ref. [38].

As long-established, the elastic moduli of bcc Fe based solid solutions are linear functions of solute content, especially at the dilute solution limit [39]. For example, the calculated bulk modulus difference, ΔB values of six Fe-X (X=Ti, V, Cr, Co, Ni, and Cu) alloys decrease linearly with increasing solute content [31]. However, we find an exceptional case in Fe-Mn alloy. As shown by the filled circle in FIG. 1(a), ΔB of Fe-Mn alloy decreases linearly when Mn concentration increases from 0.4 to 1.39 at.% (Note: we firstly focus on the ground state at 1.39 at.% Mn). However, it increases abruptly and drastically by 22.83 GPa from 1.39 to 1.85 at.% Mn, and then increases slightly by 1.5 GPa at 2.08 at.% Mn. We also find that Δa of Fe-Mn alloy anomalously decreases as Mn content increases at 1.85 at.%, as shown by the filled square in FIG. 1(b), while Δa of all other alloys increases linearly with increasing solutes in the whole range. Besides, the calculated E_{ela} and E_{sub} both exhibit discontinuous variations as Mn content increases from 1.39 to 1.85 at.%, as shown by filled symbols in FIGS. 1(c) and (d), deviating from the "common linear expectations." The abrupt increase of E_{sub} at 1.85 at.% Mn is similar to the thermodynamic anomaly of the mixing energy at ~ 1.5 at.% Mn predicted by LMTO calculations [29]. These anomalous phenomena in Fe-Mn alloy may correlate with the dual character of the $3d^5$ electrons of Mn [30], which is unique among these $3d$ solutes.

The underlying mechanisms behind these anomalous phenomena might be discovered by investigating the evolution of electronic structure with Mn concentration. Firstly, we examine the evolution of electron localization function (ELF) [40] with increasing Mn content. The ELF evolutions of six other Fe-X (X=Ti, V, Cr, Co, Ni, and Cu) alloys are also examined for comparison. The ELF values of the bonding attractors between Mn and the first, as well as the second nearest neighbors (1NNs&2NNs) are both around 0.15, indicating typical metallic bonds. In the range from 0.4 to 1.39 at.% Mn, the ELF value of bonding attractors between Mn and 1NNs is $\sim 10\%$ less than that one between Mn and 2NNs. However, they are equal at

1.85 and 2.08 at.% Mn. Figure. 2(a) shows the shrink of ELF bonding domains between Mn and 2NNs as Mn increases from 1.39 to 1.85 at.%. This reflects the relative increase of the ELF value of the bonding-attractors between Mn and 1NNs, indicating the strengthened bonding between Mn and 1NNs. In all other six Fe-X alloys, it is almost constant of the bonding-attractor ELF ratio between solute and 1NNs over that between solute and 2NNs within the whole solute concentration range. Therefore, the abrupt increases of ΔB and E_{cla} from 1.39 to 1.85 at.% Mn might be attributed to the strengthened bonding between Mn and 1NNs. Meanwhile, the increased attraction between Mn and 1NNs compresses the Fe-Mn alloy, which leads to an anomalous lattice constant decreasing over 1.39 to 1.85 at.% Mn.

Additionally, we examine the magnetism evolution in Fe-Mn alloy. The magnetic moment is calculated by using the standard Wigner-Seitz radius in the VASP pseudopotential database. Fe atoms only show a tiny variation of magnetic moment ($\sim 2.2 \mu_B$) within the whole content range of Mn. Our calculated μ_{Mn} is in good consistency with the published data [19-23,26,41], as shown in FIG. 2(b). Especially, the excited state at 1.39 at.% Mn with a small positive μ_{Mn} is consistent with the experimental result, $\sim 0 \mu_B$ [21]. The μ_{Mn} is almost constant, about $-1.8 \mu_B$, as Mn content increases from 0.4 to 1.39 at.%, but increases abruptly and drastically to be $0.313 \mu_B$ at 1.85 at.% Mn and then keeps almost constant at 2.08 at.% Mn. This suggests that solute Mn and Fe matrix are in AFM coupling from 0.4 to 1.39 at.% Mn, but in FM coupling at 1.85 and 2.08 at.% Mn, which agrees very well with experimental results [19-24]. However, in six other Fe-X (X=Ti, V, Cr, Co, Ni, and Cu) alloys, the calculated moments of solutes do not show much variation with solute content.

Consequently, it might be suggested that the Fe-Mn alloy undergoes an IPT as Mn content increases from 1.39 to 1.85 at.%, from the inversion of magnetic coupling order, the strengthening of the bonding between Mn and 1NNs, and the sudden jumps of ΔB and Δa . Interestingly, the increase of ΔB and decrease of Δa from the AFM phase to the FM phase might be intuitively explained by the atomic relaxations of the two phases presented by King *et al.* based on DFT calculations with PBE functional (see FIG. 3 in Ref. [26]). Their results show that in the AFM phase, Fe atoms in body-diagonal directions displace away from solute Mn in a rather long-range region while Fe atoms in [100] and [201] directions displace

towards solute Mn in a smaller region, which makes the lattice looser. However, in the FM phase, Fe atoms displace towards solute Mn in all directions with the largest magnitude of 1NNs [26], resulting in a more compact lattice (increased ΔB and decreased Δa). The shortened distance between Mn and 1NNs reflects the strengthened bonding in the FM phase compared with the AFM phase, showing perfect consistency with our ELF calculations. We specially calculate the external pressure at different μ_{Mn} values on $\text{Fe}_{53}\text{Mn}_1$ system (1.85 at.% Mn) with fixed volume. This volume is an equilibrium one by simultaneously optimizing ionic and magnetic configurations at zero pressure. As shown in FIG. 3(a), the external pressure decreases monotonously as μ_{Mn} increases from -2.8 to $1.7 \mu_{\text{B}}$, but increases slightly from 1.7 to $2.7 \mu_{\text{B}}$. The total energy is also calculated as a function of μ_{Mn} , showing similar trend with that of Schneider *et al.* [19]. There is a flat local minimum around $0.2 \mu_{\text{B}}$ in the curve of energy versus μ_{Mn} , which might indicate an excited state. The resulted enthalpy shows a flat bottom within μ_{Mn} range from 0.7 to $1.7 \mu_{\text{B}}$ as shown in FIG. 3(c), which explains why experiments under normal pressure always present positive μ_{Mn} at 2.0 at.% Mn and higher concentrations.

Towards a further understanding of this IPT, we examine the evolution of differential electron density ρ^{diff} in (110) plane of these solutes. Herein, ρ^{diff} is calculated by the electron density at a certain solute content subtracting that at the next lower solute content than the former, and a preprocessing is performed before the calculation [31]. There is only a slight change (within $\pm 0.02 e/\text{\AA}^3$) in (110) ρ^{diff} of solutes Ti, V, Cr, Co, Ni, and Cu, as they increase from 0.4 to 2.08 at.%. However, as shown in FIG. 4, there is a sudden electron transfer from regions along body diagonals ($[\bar{1}11]$ and equivalent directions) to regions along [001] direction within a tiny sphere (radius: $\sim 0.17a$) around solute Mn, as its content increases from 1.39 to 1.85 at.%. We find only minor changes in the numbers of s , p , and d charges of Mn and the Fermi energy E_{F} of the alloy within the whole Mn content range, indicating fixed valence of Mn. Hence, it is speculated that this electron transfer is within $3d$ states: from the itinerant t_{2g} bands (triply degenerate) along body diagonals to the localized e_g level (dually degenerate) along [001] direction [41]. To check this hypothesis, we respectively calculate the spin-polarized DOS for t_{2g} bands by averaging those of d_{zx} , d_{yz} , and d_{xy} , and for e_g level by

averaging those of d_{z^2} and $d_{x^2-y^2}$. The e_g and t_{2g} DOS curves of Mn are plotted in FIGs. 5(a) and (b). As we can see, the peaks in the downward branch of t_{2g} DOS shrink while the upward e_g peak shifts in the low-energy direction to be below E_F level from 1.39 to 1.85 at.% Mn. Our results of the shrink of t_{2g} peak and the simultaneously increased density of e_g state at E_F level are similar to the experimental observations of the shortening of the peak at around -2 eV and the simultaneously height-increasing of the peak at E_F level in the photoemission spectra during the $\gamma \rightarrow \alpha$ Ce transition [12]. These DOS curves perfectly correspond to the differential electron density observations; for example, the shift of the upward e_g peak from above E_F level to below corresponds to the electron transfer at 1.85 at.% Mn in FIG. 4. These results confirm the electron transfer from t_{2g} bands to e_g level. Rahman *et al.* also observed similar e_g peak shift in a systematic studying the DOS curves of 3d solutes in bcc Fe matrix, and explained that additional 3d electrons are forced to enter the e_g majority spin states and couple ferromagnetically to the host Fe atoms [42].

Figure 5(c) shows the proportion of e_g electrons (n_{e_g}) in the total 3d electrons as a function of Mn content, presenting an abrupt increase from 1.39 to 1.85 at.% Mn. This n_{e_g} increasing is very similar to that of $n_{a_{1g}}$ in the insulator \rightarrow metal transition of V_2O_3 calculated by the DFT method combined with dynamical mean-field theory [17]. According to these DOS curves, we plot a schematic of 3d electron transfer from the lower t_{2g} bands to the upper e_g level in FIG. 5(d), which thoroughly explains the abrupt E_{sub} increase as Mn increases from 1.39 to 1.85 at.% in FIG. 1(d).

Interestingly, according to the band structure theory suggested by Goodenough [41], it is the 3d electron transfer that gives rise to the inversion of magnetic coupling order and the concomitant Fe-Mn bond strengthening. From 0.4 to 1.39 at.% Mn, solute Mn is in AFM coupling with Fe matrix, resulting from that the e_g level is filled with very few electrons but not empty. Meanwhile, the bonding half of the t_{2g} band is filled, and the antibonding half is partially filled. As Mn increases at 1.85 at.%, the electron transfer makes the bonding half of the t_{2g} band still filled or very close to filled, but the antibonding half empty, which leads to the Fe-Mn bond strengthening. Furthermore, the upward branch of the e_g level becomes filled

or close to be filled at 1.85 at.% Mn, leading to FM coupling between Mn and Fe matrix. In this sense, the decreased occupation of the t_{2g} state corresponds to the bond strengthening between Mn and 1NNs, and the increased occupation of the e_g level corresponds to the FM coupling order. Therefore, the proportion of e_g electrons, $n_{e_g}/(n_{e_g} + n_{t_{2g}})$, might be the order parameter of this IPT.

At last, we discuss three issues. The first one is about the excited state (FM phase) at 1.39 at.% Mn. Figure S7 displays 3d DOS curves, ELF domains, and differential electron density contour (the FM phase minus the AFM phase with $\mu_{\text{Mn}} \sim -1.8 \mu_{\text{B}}$) on (110) plane of Mn [31], which are very similar to those counterparts of the FM phase at 1.85 at.% Mn. Hence, this excited state essentially possesses elastic, structural, and electronic properties of the FM phase. Our calculated E_{sub} of Mn in this excited state is ~ 0.05 eV higher than that in the AFM phase at 1.39 at.% Mn. An experimental μ_{Mn} of $\sim 0 \mu_{\text{B}}$ was observed at 1.5 at.% Mn at ambient conditions [21], which might indicate this excited state is reached although with a small probability. In addition, our calculations show that only this excited state exists under pressures above 10.0 kBar at 1.39 at.% Mn [31]. Secondly, when the $\text{Fe}_{53}\text{Mn}_1$ system is under a -2.0% volumetric strain, the two local minima, respectively, at $-1.3 \mu_{\text{B}}$ (46.4 kBar) and $0.7 \mu_{\text{B}}$ (40.3 kBar), have similar energies, as shown in FIG. 3(b). Our calculations on the $\text{Fe}_{53}\text{Mn}_1$ system show that above 37.0 kBar, the enthalpy of the FM phase is lower than the AFM phase with $\mu_{\text{Mn}} \sim -1.8 \mu_{\text{B}}$ [31]. These results demonstrate that the FM phase is the ground state under high pressure at 1.85 at.% Mn. The third issue is about the Mn-cluster effect on this IPT. We calculate ΔB at 1.56 at.% Mn by using $\text{Fe}_{126}\text{Mn}_2$ systems with various Mn-pair configurations at zero pressure [31]. The ΔB values with Mn-pairs forming from the first to the fourth nearest neighbors (1NN–4NN, see Ref. [27]) locate very close to the line of before the IPT, while that with the 5NN Mn-pair locates on the line of after the IPT, as shown in FIG. S10 in Ref. [31]. For the configurations in which the Mn-pair lengths are farther than that of 5NN, *ab initio* calculations cannot converge under the prescribed force criterion (≤ 0.002 eV/Å per atom). Nonetheless, under a relaxed criterion, ≤ 0.004 eV/Å per atom, the calculations converge only for two configurations: "far1" denoting the [100] Mn-pair of $2a$ length, and "far2" denoting the [111] Mn-pair of $2\sqrt{3}a$ length. As can be seen, ΔB values of "far1" and

"far2" respectively locate close to lines of after and before the IPT. From these results, it can be concluded that the $\text{Fe}_{126}\text{Mn}_2$ systems with Mn-pair configurations of 5NN and "far1" are both in the FM phase.

In summary, our DFT calculations using dense k -point meshes describe two distinct solutions (phases) of dilute bcc Fe-Mn alloys and capture an iso-structural phase transition (IPT) between them. This IPT originates from the main peak of $3d e_g$ state shifting across the Fermi level. The mechanisms emphasize that the dual character of $3d^5$ electrons of Mn is driven by an intra-atomic electron transfer between the itinerant t_{2g} band and the localized e_g level. This IPT can be induced by changing Mn content or external pressure. The phase transition implies a sudden jump of bulk modulus, an inversion of magnetic coupling order between solute Mn and Fe matrix, and a change of bonding strength between Mn and its first-nearest neighboring Fe atoms. Our study provides a full view of the electronic process of this IPT, which is enlightening for understanding the mechanisms of other similar correlation-driven phase transitions. Our results also indicate that bcc Fe-Mn alloy might have a more complex phase diagram than what is already known.

This work is supported by the National Key Research and Development Program of China (Grant Nos.: 2017YFE0302400, 2017YFA0402800 and 2016YFE0120900), the National Natural Science Foundation of China (Nos.: 11735015, 51571187, 51871207, 51671185, 11874192, 21463025, and U1832206). C.R. Miranda acknowledges the financial support provided by the Brazilian Ministry of Science and Technology for collaborative research between China and Brazil, and the Brazilian funding agencies National Council of Scientific and Technologic Development (CNPq), and Fundação de Amparo à Pesquisa do Estado de São Paulo (FAPESP).

References

- [1] A. Jayaraman, Phys. Rev. **137**, A179 (1965).
- [2] J. R. Salvador, F. Guo, T. Hogan, M. G. Kanatzidis, Nature **425**, 702 (2003).
- [3] S. Lee, A. Pirogov, M. Kang, *et al.*, Nature **451**, 805 (2008).
- [4] R. J. Zeches, M. D. Rossell, J. X. Zhang, *et al.*, Science **326**, 977 (2009).

- [5] J. F. Scott, Adv. Mater. **22**, 2106 (2010).
- [6] M. Krisch, D. L. Farber, R. Xu, D. Antonangeli, *et al.*, Proc. Natl. Acad. Sci. USA **108**, 9342 (2011).
- [7] H. Sato, K. Shimada, M. Arita, *et al.*, Phys. Rev. Lett. **93**, 246404 (2004).
- [8] C. U. Segre, M. Croft, J. A. Hodges, V. Murgai, L. C. Gupta, R. D. Parks, Phys. Rev. Lett. **49**, 1947 (1982).
- [9] J. M. D. Coey, S. K. Ghatak, M. Avignon, F. Holtzberg, Phys. Rev. B **14**, 3744 (1976).
- [10] A. Jayaraman, D. B. McWhan, J. P. Remeika, P. D. Dernier, Phys. Rev. B **2**, 3751 (1970).
- [11] U. Kornstädt, R. Lässer, B. Lengeler, Phys. Rev. B **21**, 1898 (1980).
- [12] L. Z. Liu, J.W. Allen, O. Gunnarsson, N. E. Christensen, O. K. Andersen, Phys. Rev. B **45**, 8934 (1992).
- [13] A. V. Nikolaev, K. H. Michel, Phys. Rev. B **66**, 054103 (2002).
- [14] M. Casadei, X. Ren, P. Rinke, A. Rubio, M. Scheffler, Phys. Rev. Lett. **109**, 146402 (2012).
- [15] N. Devaux, M. Casula, F. Decremps, S. Sorella, Phys. Rev. B **91**, 081101(R) (2015).
- [16] M. Casadei, X. Ren, P. Rinke, A. Rubio, M. Scheffler, Phys. Rev. B **93**, 075153 (2016).
- [17] M. S. Laad, L. Craco, E. Müller-Hartmann, Phys. Rev. Lett. **91**, 156402 (2003).
- [18] I. Lo Vecchio, J. D. Denlinger, O. Krupin, *et al.*, Phys. Rev. Lett. **117**, 166401 (2016).
- [19] A. Schneider, C.-C. Fu, C. Barreteau, Phys. Rev. B **98**, 094426 (2018).
- [20] F. Kajzar, G. Parette, Phys. Rev. B **22**, 5471 (1980).
- [21] M. F. Collins, G. G. Low, Proc. Phys. Soc. **86**, 535 (1965).
- [22] H. R. Child, J. W. Cable, Phys. Rev. B **13**, 227 (1976).
- [23] P. Radhakrishna, F. Livet, Solid State Commun. **25**, 597 (1978).
- [24] Y. Nakai, N. Kunitomi, J. Phys. Soc. Jpn. **39**, 1257 (1975).
- [25] V. I. Anisimov, V. P. Antropov, A. I. Liechtenstein, V. A. Gubanov, A. V. Postnikov, Phys. Rev. B **37**, 5598 (1988).
- [26] D. J. M. King, S. C. Middleburgh, P. A. Burr, T. M. Whiting, P. C. Fossati, M. R. Wenman, Phys. Rev. B **98**, 024418 (2018).
- [27] P. Olsson, T. P. C. Klaver, C. Domain, Phys. Rev. B **81**, 054102 (2010).
- [28] N. I. Kulikov, C. Demangeat, Phys. Rev. B **55**, 3533 (1997).

- [29] A. A. Mirzoev, M. M. Yalalov, D. A. Mirzaev, *Phys. Met. Metallogr.* **101**, 341 (2006).
- [30] J. L. Smith, E. A. Kmetko, *J. Less-common Metals* **90**, 83 (1983).
- [31] See Supplementary Material in the same Submission, which includes additional information on: (i) bulk modulus variation with solute content of 7 Fe-X (X=3d transition metals) alloys; (ii) determination of magnetic coupling phase at 6 Mn concentrations; (iii) electronic and magnetic properties of the ferromagnetic phase at 1.39 at.% Mn; (iv) enthalpy variation with pressure of Fe₅₃Mn₁ system in ferromagnetic phase; (v) elastic, structural and magnetic properties of Fe₁₂₆Mn₂ system.
- [32] G. Kresse, J. Hafner, *Phys. Rev. B* **47**, 558(R) (1993).
- [33] G. Kresse, J. Furthmüller, *Phys. Rev. B* **54**, 11169 (1996).
- [34] J. P. Perdew, J. A. Chevary, S. H. Vosko, *et al.*, *Phys. Rev. B* **46**, 6671 (1992).
- [35] S. H. Vosko, L. Wilk, M. Nusair, *Can. J. Phys.* **58**, 1200 (1980).
- [36] W. Liu, X. Wu, X. Li, *et al.*, *Comput. Mater. Sci.* **96**, 117 (2015).
- [37] L. Qi, D. C. Chrzan, *Phys. Rev. Lett.* **112**, 115503 (2014).
- [38] W. Liu, W. L. Wang, Q. F. Fang, *et al.*, *Phys. Rev. B* **84**, 224101 (2011).
- [39] W. C. Leslie, *Metall. Trans.* **3**, 5 (1972).
- [40] B. Silvi, A. Savin, *Nature* **371**, 683 (1994).
- [41] J. B. Goodenough, *Phys. Rev.* **120**, 67 (1960).
- [42] G. Rahman, I. G. Kim, H. K. D. H. Bhadeshia, A. J. Freeman, *Phys. Rev. B* **81**, 184423 (2010).

Captions:

TABLE I: Solute contents (at.%) of six solid-solution systems, dimensions, and corresponding k -point meshes. All k -point meshes are Γ -centered. For the first five supercells, dimensions are in multiples l , m , and n of a two-atom bcc cell respectively along $[100]$, $[010]$ and $[001]$ directions; for the last supercell, dimensions are in multiples l , m , and n of a four-atom tetragonal cell (see FIG. 1(a) in Ref. [37]) respectively along $[100]$, $[011]$ and $[0\bar{1}1]$ directions. Herein X denotes solute; l , m , and n are integers. It is also shown the calculated lattice constant a_0 (unit: Å) and bulk modulus B (unit: GPa) of α -Fe at each set of supercell and k -point mesh. The effect of Pulay stress on a_0 and B is corrected [31].

FIG. 1. (Color online) Variations of (a) bulk modulus change ΔB , (b) lattice constant change Δa , (c) elastic energy E_{ela} , and (d) substitution energy E_{sub} as Mn content increases. The excited state at 1.39 at.% Mn is represented by half-filled symbols. Lines are linear fits. The E_{ela} values are for systems with 250 atoms at each Mn content.

FIG. 2. (Color online) (a) Domains of electron localization function (ELF) between Mn (purple ball at center) and the first, as well as the second nearest neighbors (1NNs&2NNs, brown balls; but 2NNs are not shown) respectively at 1.39 and 1.85 at.% Mn. The left picture is the case of antiferromagnetic phase at 1.39 at.% Mn. The ELF value is set to be that of the attractors between Mn and 1NNs. (b) The magnetic moment of Mn (μ_{Mn}) versus its content. The excited state at 1.39 at.% Mn is represented by the half-filled circle. The published data are from Refs. [19,21,22,26,27,41].

FIG. 3. (Color online) (a) External pressure (P), (b) relative total energy (ΔE) and (c) relative enthalpy (ΔH) as a function of magnetic moment of Mn in $\text{Fe}_{53}\text{Mn}_1$ system. Red open square and blue open circle respectively denote results at equilibrium volume and at volumetric strain of -2.0% . The ΔE and ΔH values are respectively relative to those at -1.3 and $1.2 \mu_{\text{B}}$. Thin broken horizontal lines denote the altitudes of local minima.

FIG. 4. (Color online) Differential electron density on the (110) plane of Mn in bcc Fe-Mn alloy from 0.4 to 2.08 at. % Mn. The unit of electron density is $e/\text{\AA}^3$. In all pictures, Mn atoms

are placed at the center. In the leftmost picture, the four black dots mark the first nearest neighbor Fe (1NN).

FIG. 5. (Color online) Spin-polarized DOS curves of (a) $3d t_{2g}$ and (b) $3d e_g$ states of Mn at different Mn content. At 1.39 at.% Mn, only the antiferromagnetic DOS curves are shown. (c) The proportion of e_g electron number to the total $3d$ electron number as a function of Mn content. (d) Schematic of electron transfer within $3d$ states. The blue arrow indicates the electron transfer direction. The magenta and red arrows respectively denote the upward spin of e_g state and downward spin of t_{2g} state.

TABLE I

at.% X	system	dimension	k -point mesh	system	a_0	B
0.40	$\text{Fe}_{249}\text{X}_1$	$5 \times 5 \times 5$	4^*4^*4	Fe_{250}	2.8325	189.65
0.78	$\text{Fe}_{127}\text{X}_1$	$4 \times 4 \times 4$	5^*5^*5	Fe_{128}	2.8326	190.15
1.04	Fe_{95}X_1	$4 \times 4 \times 3$	5^*5^*7	Fe_{96}	2.8322	191.65
1.39	Fe_{71}X_1	$3 \times 3 \times 4$	7^*7^*5	Fe_{72}	2.8319	193.15
1.85	Fe_{53}X_1	$3 \times 3 \times 3$	7^*7^*7	Fe_{54}	2.8314	193.32
2.08	Fe_{47}X_1	$3 \times 2 \times 2$	7^*10^*10	Fe_{48}	2.8308	193.15

FIG. 1

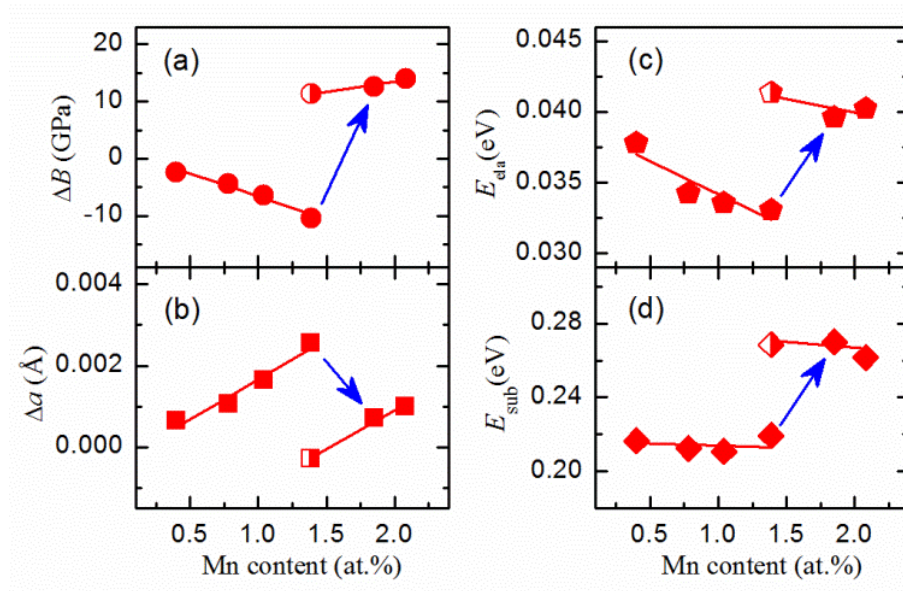


FIG. 2

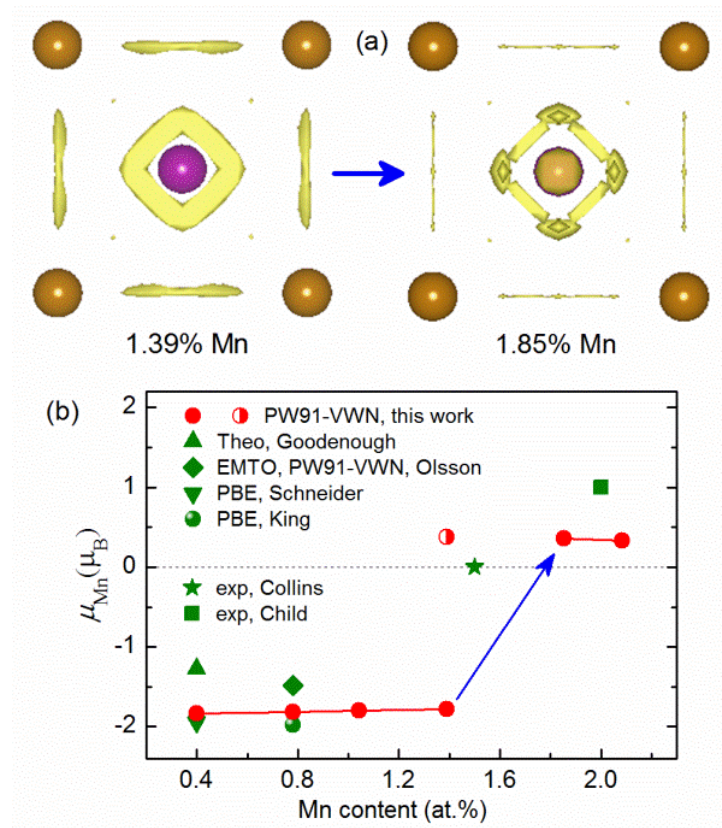


FIG. 3

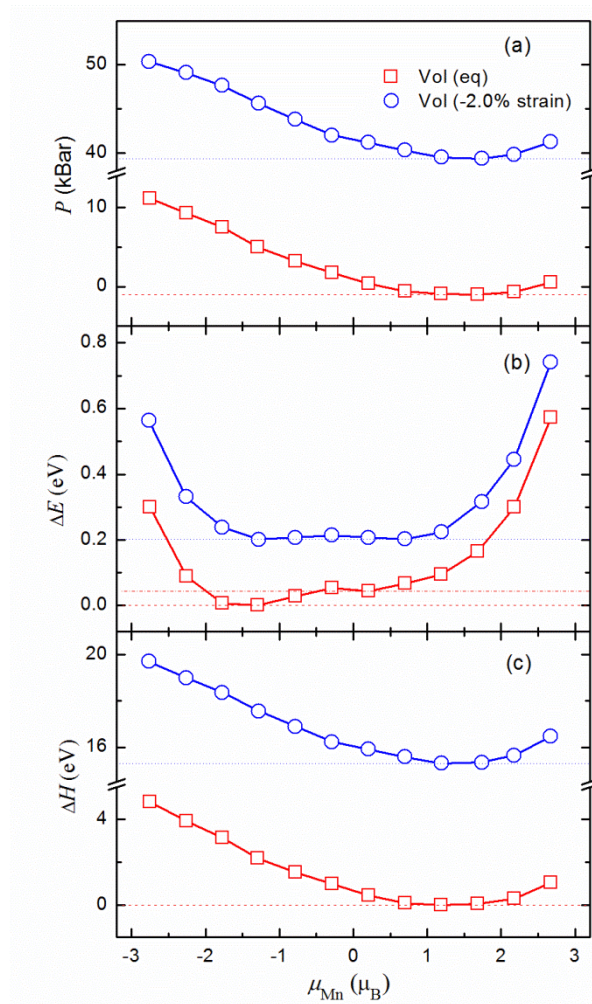


FIG. 4

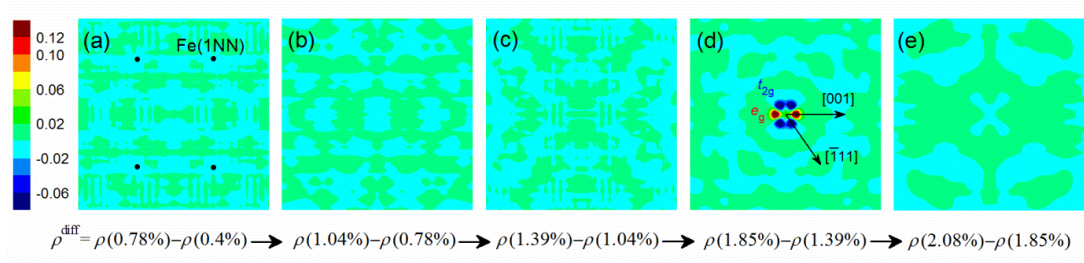


FIG. 5

